J. Fluid Mech. (1988), *vol.* 188, *pp.* 275–300
Printed in Great Britain

The flow of a liquid film along a periodic wall

By C. POZRIKIDIS
Department of Applied Mechanics and Engineering Sciences, B-010, University of California, San Diego, La Jolla, CA 92093, USA

(Received 27 January 1987 and in revised form 17 August 1987)

The creeping flow of a liquid film along an inclined periodic wall of arbitrary geometry is considered. The problem is formulated using the boundary-integral method for Stokes flow. This method is extended to two-dimensional flows involving free surfaces, and is implemented in an iterative numerical procedure. Detailed calculations for flow along a sinusoidal wall are perfomed. The free-surface profile is studied as a function of flow rate, inclination angle, wave amplitude, and surface tension, and is compared with previous asymptotic solutions. The results include streamline patterns, velocity profiles and wall-shear-stress distributions, and establish criteria for flow reversal. For specified wall geometry, the asymptotic behaviour for very small flow rates is shown to be a strong function of surface tension. It is demonstrated that these results are valid in a qualitative sense for general wall geometries. The analogy between gravity-driven flow and the flow of a liquid layer on a rotating disk (spin coating) is also discussed.

1. Introduction

An important class of problems in fluid mechanics involves viscous flows in the presence of free surfaces or fluid interfaces. The deformation of bubbles or drops in specified flows provides a widely studied example with a variety of technological applications. In more complicated situations, these flows may be affected by the presence of solid, elastic or viscoelastic boundaries, as is the case in various coating or extrusion operations. Furthermore, these flows often occur simultaneously with phase-change phenomena, chemical reactions and heat or mass transfer affecting the rate of these processes. Examples from the field of chemical engineering include electrochemical plating, chemical etching, crystal growth, and chemical conversion in liquid–gas catalytic reactors.

The mathematical analysis of steady free-surface flows becomes complicated by the fact that the location of the free-surface is not known *a priori*, but has to be found as part of the solution. This makes the problem highly nonlinear requiring special mathematical treatment. One may derive asymptotic solutions for flows that deviate slightly from known simple configurations, but in the general case, one has to rely on numerical solutions. The analysis of transient or unsteady flows on the other hand requires the tracking of Lagrangian lines that coincide with free surfaces or fluid interfaces. This necessitates the development of numerical techniques that are based on a Lagrangian formulation, or combine a Lagrangian with an Eulerian description.

Before considering our specific problem it is appropriate to review available numerical techniques for treating free-surface flow problems. In the following discussion we use the term free surface to include both free surfaces and fluid interfaces. Confining ourselves to viscous flows, we find three general lines of

approach characterized by boundary-integral, finite-difference, and finite-element formulations. In the first case, which is applicable only for Stokes flow, the free surface constitutes a flow boundary and hence its evolution is pursued in a straightforward fashion (Kelmanson 1983; Rallison 1984; Geller, Lee & Leal 1986). The situation is more complicated when finite-difference or finite-element formulations are employed, for the free surface may intersect the underlying grid. Here one has several choices including the use of boundary-fitted coordinate systems (Ryskin & Leal 1984*a–c*) or adaptive grids (see for instance Kistler & Scriven 1983), formulation in terms of Lagrangian dynamics (Hirt, Cook & Butler 1970), and the use of free-surface or fluid-volume marker points (Hirt & Nichols 1981). It is important to bear in mind that the above methods were developed with reference to specific physical problems, and thus they are most effective in different physical contexts.

In the present article we consider the flow of a liquid film along a periodic solid wall that is driven by a uniform force field. Previous studies on this topic concentrated mainly on the simple but non-trivial case of flow down an inclined, perfectly plane wall. There are a number of experimental and theoretical efforts that consider the stability of this flow or address the onset of steady, periodic or solitary, finite-amplitude waves (Krantz & Goren 1970; Chin, Abernathy & Bertchy 1986). In addition, there are numerous experimental studies addressing the effect of wall roughness on the critical Reynolds number for transition to turbulence, and on the rate of simultaneous heat or mass transfer. Early work in this area is summarized in a comprehensive review article by Fulford (1964, §IV–E). Studies of flow along corrugated walls are limited to a few asymptotic analyses, including the study of the linear stability and weakly nonlinear waves on film flow down an inclined uneven wall (Tougou 1978), the analysis of flow along a sinusoidal wall with small-amplitude striations (Wang 1981; Dassori, Deiber & Cassano 1984), and the analysis of flow of a very thin film along a curved wall (Wang 1984). We are concerned with the more general case of finite-amplitude corrugations and, more importantly, with walls of generalized geometry. Specifically, we address how the wall geometry affects the free-surface profile and the structure of the flow, with emphasis on flow reversal and wall-sheer-stress distribution. Furthermore, we examine the significance of surface tension, and discuss the implications of our results on simultaneous molecular–convective processes.

For the analysis of our flow of interest we choose to employ the boundary-integral method for Stokes flow. The numerical procedure requires the calculation of only the boundary values of the stress and velocity, along with the unknown free-surface profile. This formulation lowers the dimension of the computational domain with respect to that of the physical domain by one, and thus significantly reduces the computational effort. Employing the boundary-integral method restricts the validity of our results to conditions of creeping motion (requiring either a low body-force environment or moderate flow rates), but allows an accurate and detailed investigation.

It is important to note that although the boundary-integral method has been extensively used to study axisymmetric or genuinely three-dimensional problems with free surfaces (Rallison 1984), it has only recently been applied to two-dimensional flows (Kelmanson 1983). This is perhaps due to certain inherent mathematical difficulties encountered in two dimensions, as discussed by Higdon (1985). Kelmanson (1983) considers the biharmonic equation (satisfied by the stream function), and uses the stream function and vorticity as primary variables. We prefer

to follow the velocity–force formulation, for this offers additional advantages of straightforward extension to three dimensions, and leads to direct evaluation of quantities of primary importance. Furthermore, we devote a significant part of our effort to the development, implementation, and evaluation of various iteration techniques including the ones used by previous authors. We felt that this was a necessary task before any extensive computations were made. Overall, the proposed method, combined with those of Higdon (1985) and Lee & Leal (1986), provide a complete description of the boundary-integral method for two-dimensional internal, external, semi-infinite, and free-surface flows.

2. Formulation

We consider the slow flow of a liquid film along an inclined two-dimensional periodic wall, as illustrated in figure 1. At very low Reynolds numbers the flow is governed by the Stokes equation, with the body-force term included,

$$-\frac{\partial P}{\partial x_i}+\mu\frac{\partial^2 u_i}{\partial x_j\,\partial x_j}+\rho g_i = 0, \tag{1}$$

and the continuity equation,

$$\frac{\partial u_i}{\partial x_i} = 0. \tag{2}$$

For the mathematical analysis, it is convenient to decompose the flow into a basic and a disturbance component, denoted by a tilde and an overbar respectively, $u_i = \tilde{u}_i + \bar{u}_i$, $P = \tilde{P} + \bar{P}$, such that

$$-\frac{\partial \tilde{P}}{\partial x_i}+\mu\frac{\partial^2 \tilde{u}_i}{\partial x_j\,\partial x_j}+\rho g_i = 0, \tag{3}$$

$$-\frac{\partial \bar{P}}{\partial x_i}+\mu\frac{\partial^2 \bar{u}_i}{\partial x_j\,\partial x_j} = 0. \tag{4}$$

Both components satisfy the continuity equation. For the disturbance flow we use the reciprocal theorem to express the flow as a function of the boundary velocity and boundary force, $\bar{f}_i = \bar{\sigma}_{ij} n_j$, where $\bar{\sigma}_{ij}$ is the stress tensor,

$$\bar{\sigma}_{ij} = -\delta_{ij}\bar{P}+\mu\left(\frac{\partial \bar{u}_i}{\partial x_j}+\frac{\partial \bar{u}_j}{\partial x_i}\right),$$

and n_j is the unit normal to the boundary pointing into the fluid (Pozrikidis 1987). The result for points on the boundary is

$$\bar{u}_j(\boldsymbol{x}_0) = \frac{1}{2\pi\mu}\int_B [\bar{f}_i(\boldsymbol{x})\, S_{ij}(\boldsymbol{x}_0, \boldsymbol{x}) - \bar{u}_i(\boldsymbol{x})\, G_{ij}(\boldsymbol{x}_0, \boldsymbol{x})]\, \mathrm{d}S(\boldsymbol{x}), \tag{5}$$

where the integration is over all solid, free, and liquid flow boundaries. For points within the flow domain, the factor $\frac{1}{2\pi\mu}$ must be replaced by $\frac{1}{4\pi\mu}$.

The tensor S_{ij} constitutes a fundamental solution to Stokes equation representing an array of point forces along the x-axis,

$$\boldsymbol{S}(\hat{x}) = \begin{pmatrix} A+k\hat{y}A_y & -k\hat{y}A_x \\ -k\hat{y}A_x & A+1-k\hat{y}A_y \end{pmatrix}, \tag{6}$$

where

$$A = \tfrac{1}{2}\ln\,[2(\cosh(k\hat{y})-\cos(k\hat{x}))]+c,$$

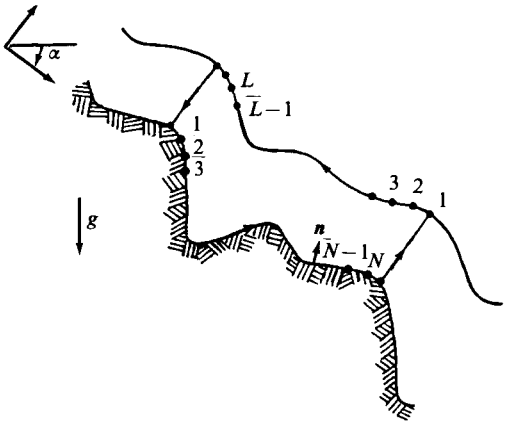

FIGURE 1. Flow of a liquid film along a periodic solid wall: schematic representation.

$\hat{\boldsymbol{x}} = \boldsymbol{x} - \boldsymbol{x}_0$, and c is an arbitrary constant (Pozrikidis 1987). $G_{ij} = \tau_{ijk} n_k$, where the tensor τ_{ijk} expresses the stress associated with the above fundamental solution,

$$\left.\begin{aligned} \tau_{xxx} &= 2\mu \operatorname{div}(A, k\hat{y}A_x), \\ \tau_{xxy} &= 2\mu \operatorname{div}(-k\hat{y}A_x, A), \\ \tau_{xyy} &= 2\mu \operatorname{div}(A, -k\hat{y}A_x), \\ \tau_{yyy} &= 2\mu \operatorname{div}(k\hat{y}A_x, A), \\ \tau_{ijk} &= \tau_{kij} = \tau_{jki}. \end{aligned}\right\} \tag{7}$$

For non-periodic flows or flows having specific symmetries, other fundamental solutions may be employed as discussed by Pozrikidis (1987).

Equation (5) is an integral equation of the first kind for the boundary force and of the second kind for the boundary velocity. It is highly nonlinear with respect to the free-surface profile.

For the boundary conditions, we require the no-slip condition along the solid wall

$$u_i = 0, \quad \text{or } \bar{u}_i = -\tilde{u}_i, \tag{8}$$

and zero normal velocity along the free surface,

$$u_i n_i = 0, \quad \text{or } \bar{u}_N = \bar{u}_i n_i = -\tilde{u}_i n_i. \tag{9}$$

For flow without surfactants we also require zero shear stress along the free surface,

$$\sigma_{sh} = \sigma_{ij} n_j t_i = 0, \tag{10}$$

where t_i is the unit tangent to the free surface; and a condition for the normal stress involving capillary forces

$$\sigma_N = \sigma_{ij} n_j n_i = -P^0 + \frac{\sigma}{R}, \tag{11}$$

where P^0 is a reference external pressure, σ is the surface-tension coefficient, and R is the radius of curvature at the boundary. Using the last two equations, we may derive boundary conditions for the disturbance boundary force at the free surface

$$\bar{f}_i = \left(-P^0 + \frac{\sigma}{R}\right) n_i - \tilde{\sigma}_{ij} n_j. \tag{12}$$

Defining the flow domain as equal to one flow period, let us integrate (5) over the contour indicated in figure 1. Owing to the periodicity of the fundamental solution, the contribution from the straight segments vanishes and, thus, the disturbance velocity is expressed as an integral over the solid wall W and the free surface S.

For specified wall shape, liquid flow rate, and surface-tension coefficient, the problem is then to solve (5) for the disturbance force along the solid wall, the disturbance tangential velocity along the free surface, and the free-surface profile, subject to the boundary conditions (8)–(12).

3. Numerical procedure

Having formulated the problem as a nonlinear integral equation (the nonlinearity arising through the unknown free-surface profile), we now consider an iterative solution procedure. At the outset, it is useful to review possible strategies and to formulate them in the context of the boundary-integral method.

In general, for the iterative solution of steady free-surface problems, two main strategies may be adopted. In the first, one implements all boundary conditions into the governing equations and solves the resulting system. In the second, one implements only part of the boundary conditions, and solves the resulting system using the remaining boundary conditions as constraints. The success and efficiency of each strategy depends on the geometry of the problem as well as on the values of the dimensionless parameters characterizing the flow.

To illustrate the above procedures, let us describe the solid wall and the free surface by two sets of nodal points, x_n $(n = 1, \ldots, N)$ and x_l $(l = 1, \ldots, L)$ respectively (figure 1). In a linear approximation, we assume that both the solid wall and the free surface are polygonal lines connecting adjacent nodal points. Further, we assume that the tangential velocity at the free surface and the wall force are constant over each segment and equal to $\bar{u}_{\mathrm{T}}^l$ and $\bar{f}_i^n$ respectively.

In the first strategy (strategy A), we substitute all boundary conditions (8)–(12) into (5) to obtain the equation

$$\bar{u}_j(\boldsymbol{x}_0) + B_j(\boldsymbol{x}_0) = \bar{f}_i^n C_{ij}^n(\boldsymbol{x}_0) - \bar{u}_{\mathrm{T}}^l D_j^l(\boldsymbol{x}_0), \tag{13}$$

where

$$B_j(\boldsymbol{x}_0) = \frac{1}{2\pi\mu}\int_W \bar{u}_i G_{ij}\,\mathrm{d}S - \frac{1}{2\pi\mu}\int_S \bar{f}_i S_{ij}\,\mathrm{d}S + \frac{1}{2\pi\mu}\int_S \bar{u}_{\mathrm{N}} n_i G_{ij}\,\mathrm{d}S,$$

$$C_{ij}^n(\boldsymbol{x}_0) = \frac{1}{2\pi\mu}\int_{W_n} S_{ij}(\boldsymbol{x}_0, \boldsymbol{x})\,\mathrm{d}S,$$

$$D_j^l(\boldsymbol{x}_0) = \frac{1}{2\pi\mu}\int_{S_l} t_i G_{ij}(\boldsymbol{x}_0, \boldsymbol{x})\,\mathrm{d}S,$$

and the Einstein summation convention is implied for the superscripts n and l. W_n and S_l indicate integration over the nth wall segment and the lth free-surface segment respectively. Note that for a specified flow geometry, $B_j(\boldsymbol{x}_0)$ can be immediately evaluated using (8)–(12). To solve for the unknowns, we employ a collocation method and apply (13) at the middle of each wall segment, $\boldsymbol{x}_m$, to obtain

$$\bar{u}_j(\boldsymbol{x}_m) + B_j(\boldsymbol{x}_m) = \bar{f}_i^n C_{ij}^n(\boldsymbol{x}_m) - \bar{u}_{\mathrm{T}}^l D_j^l(\boldsymbol{x}_m), \tag{14}$$

where $m = 1, \ldots, N$. Similarly, we apply (13) at the middle of each free-surface segment, $\boldsymbol{x}_k$, to obtain

$$\bar{u}_{\mathrm{N}}(\boldsymbol{x}_k)\, n_j(\boldsymbol{x}_k) + B_j(\boldsymbol{x}_k) = \bar{f}_i^n\, C_{ij}^n(\boldsymbol{x}_k) - \bar{u}_{\mathrm{T}}^l [D_j^l(\boldsymbol{x}_k) + t_j(\boldsymbol{x}_k)\, \delta_{kl}], \tag{15}$$

where $k = 1, \ldots, L$. Equations (14) and (15) provide a system of $2(N+L)$ algebraic equations, linear with respect to the $2N$ wall forces and the L free-surface tangential velocities. It is highly nonliner with respect to the *a priori* unknown free-surface profile, as described by $\boldsymbol{x}_l$ ($l = 1, \ldots, L$). To solve this system, we introduce the discrete function $y_l(x_l)$, where x_l ($l = 1, \ldots, L$) are fixed, and specify $y_1(x_1)$ as a measure of flow rate. This provides an additional $L-1$ unknowns, namely y_l ($l = 2, \ldots, L$) raising the total number of unknowns to $2(N+L)-1$. The solution may be found by solving a set of $2(N+L)-1$ equations using Newton's method or other techniques. In particular, to implement Newton's method we transfer all terms in (14) and (15) into the right-hand side to obtain the set

$$F_{mj}(\boldsymbol{x}_m; \bar{f}_i^n, \bar{u}_{\mathrm{T}}^l, y_l) = 0, \quad F_{kj}(\boldsymbol{x}_k; \bar{f}_i^u, \bar{u}_{\mathrm{T}}^l, y_l) = 0. \tag{16}$$

Newton's method proceeds by guessing initial values for the unknowns, i.e. the wall force, the tangential velocity, and the free-surface profile, and iterating using the Jacobian matrix. Evaluation of this matrix requires calculation of the derivatives $\partial F_{pj}/\partial \bar{f}_i^n$, $\partial F_{pj}/\partial \bar{u}_{\mathrm{T}}^l$ and $\partial F_{pj}/\partial y_l$; the first two are equal to C_{ij}^n and $-D_j^l$ or $-(D_j^l + t_j\, \delta_{pl})$, whereas the third must be calculated by means of numerical differentiation.

To reduce the computational effort, variations of the above procedure may be considered. For example, one may assume that the value of F_{pj} at the point $\boldsymbol{x}_p$, is much more sensitive to $\boldsymbol{x}_p$ itself rather than to the overall free-surface shape, i.e.

$$\frac{\partial F_{pj}}{\partial y_l} \approx \frac{\partial F_{pj}}{\partial \boldsymbol{x}_p} \frac{\partial \boldsymbol{x}_p}{\partial y_l}, \tag{17}$$

where $\partial F_{pj}/\partial \boldsymbol{x}_p$ is a Fréchet derivative. This makes the Jacobian matrix sparse, reducing the numerical work by a factor of $1/(N+L)$ (a similar procedure was successfully used by Pierrehumbert (1980) for the calculation of steady, translating vortex pairs in irrotational flow). However, unfortunately, test calculations showed that for our viscous flow, this assumption is not accurate and the full Jacobian matrix must be taken into consideration.

As a second variation, one may exploit the linearity of the governing equations with respect to boundary force and velocity, to reduce the size of the final nonlinear system. Specifically, in a procedure similar to that employed by Youngren & Acrivos (1976), one may arbitrarily select from (14) and (15) two independent sets of $2N+L$ equations, and solve them with respect to the wall force and free-surface tangential velocity. Let us denote the two solutions by $(\bar{u}_{\mathrm{T}}^l)_1$, $(\bar{f}_i^n)_1$ and $(\bar{u}_{\mathrm{T}}^l)_2$, $(\bar{f}_i^n)_2$, and form the L residuals $\Delta \bar{u}_{\mathrm{T}}^l = (\bar{u}_{\mathrm{T}}^l)_1 - (\bar{u}_{\mathrm{T}}^l)_2$, and the $2N$ residuals $\Delta \bar{f}_i^n = (\bar{f}_i^n)_1 - (\bar{f}_i^n)_2$. Requiring that $L-1$ of these residuals vanish as functions of $y_l(x_l)$ ($l = 2, \ldots, L$) provides a nonlinear system of reduced order. It is clear however that the efficiency of this method must depend on the choice of the selected linear systems, as well as on the choice of residuals comprising the final nonlinear system. Other variations may be devised, but eventually the problem will always be reduced to the solution of a system of $L-1$ nonlinear equations.

Considering now the second main strategy (strategy B), we impose on (5) only three of the four boundary conditions (8)–(11). To demonstrate the procedure, let us maintain the above discretization, but, in addition, let us assume that the total

normal stress is constant over each free-surface segment, equal to σ_{N}^l, and treat it as unknown. Using (8), (9) and (10), we then write (5) in the discrete form

$$\bar{u}_j(\boldsymbol{x}_0)+F_j(\boldsymbol{x}_0)=\bar{f}_i^n\,C_{ij}^n(\boldsymbol{x}_0)-\bar{u}_{\mathrm{T}}^l\,D_j^l(\boldsymbol{x}_0)+\sigma_{\mathrm{N}}^l\,E_j^l(\boldsymbol{x}_0), \tag{18}$$

where

$$F_j(\boldsymbol{x}_0)=\frac{1}{2\pi\mu}\int_W \bar{u}_i G_{ij}\,\mathrm{d}S+\frac{1}{2\pi\mu}\int_S \tilde{\sigma}_{ik}\,n_k S_{ij}\,\mathrm{d}S+\frac{1}{2\pi\mu}\int_S \bar{u}_{\mathrm{N}}\,n_i G_{ij}\,\mathrm{d}S,$$

$$E_j^l(\boldsymbol{x}_0)=\frac{1}{2\pi\mu}\int_{S_l} n_i\,S_{ij}(\boldsymbol{x}_0,\boldsymbol{x})\,\mathrm{d}S.$$

Applying this equation at the wall collocation points yields

$$\bar{u}_j(\boldsymbol{x}_m)+F_j(\boldsymbol{x}_m)=\bar{f}_i^n\,C_{ij}^n(\boldsymbol{x}_m)-\bar{u}_{\mathrm{T}}^l\,D_j^l(\boldsymbol{x}_m)+\sigma_{\mathrm{N}}^l\,E_j^l(\boldsymbol{x}_m), \tag{19}$$

where $m=1,\ldots,N$, and at the free-surface collocation points

$$\bar{u}_{\mathrm{N}}(\boldsymbol{x}_k)\,n_j(\boldsymbol{x}_k)+F_j(\boldsymbol{x}_k)=\bar{f}_i^n\,C_{ij}^n(\boldsymbol{x}_k)-\bar{u}_{\mathrm{T}}^l[D_j^l(\boldsymbol{x}_k)+t_j(\boldsymbol{x}_k)\,\delta_{kl}]+\sigma_{\mathrm{N}}^l\,E_j^l(\boldsymbol{x}_k), \tag{20}$$

where $k=1,\ldots,L$. Now we have a linear system of $2(N+L)$ algebraic equations in $2(N+L)$ unknowns, namely $2N$ wall forces, L free-surface tangential velocities, and L free-surface normal stresses. The fact that the stress normal to the free surface may be defined within an arbitrary constant (equal to the external pressure) suggests that only $2(N+L)-1$ of these unknowns are independent. In our procedure, we specify the normal stress along the L free-surface segment, equal to $\sigma_{\mathrm{N}}^L=-P^0+\sigma/R(\boldsymbol{x}_L)$, and solve an arbitrary set of $2(N+L)-1$ equations from the above system for the remaining $2(N+L)-1$ unknowns. Imposing boundary condition (11), we then form the residual normal stresses

$$\Delta\sigma_{\mathrm{N}}^l=\sigma_{\mathrm{N}}^l+P^0-\frac{\sigma}{R}, \tag{21}$$

$l=1,\ldots,(L-1)$, where obviously $\Delta\sigma_{\mathrm{N}}^L=0$, and adjust the free-surface nodal points $y_l(x_l)$ $(l=2,\ldots,L)$ to make these residuals vanish. As previously, this may be accomplished using Newton's method or other heuristic schemes. For example, in the calculations of Ryskin & Leal (1984*a*) the free-surface points are moved by an amount proportional to the local residual normal stress, in a direction normal to the current free surface.

In a procedure completely analogous to the above, one may choose to impose the normal-stress condition at the free surface (11), and instead, to iterate using the condition of zero shear stress (10). Similarly, one may choose to satisfy both dynamic conditions (10), (11) at the free surface, and to iterate by treating the velocity normal to the free surface as unknown, i.e. using the kinematic condition (9), $\bar{u}_{\mathrm{N}}^l(y_2,y_3,\ldots,y_L)=0$. In fact, the problem may be formulated as a transient one, where the flow slowly evolves towards an asymptotic steady configuration (Rallison & Acrivos 1978). Although these methods appear viable, they were not considered in our calculations.

Having calculated the free-surface profile, free-surface velocity, and wall force, we may evaluate the velocity within the flow using a discrete form of (5),

$$\bar{u}_j(\boldsymbol{x}_0)=-\frac{1}{4\pi\mu}\int_W \bar{u}_i G_{ij}\,\mathrm{d}S-\frac{1}{4\pi\mu}\int_S\left[\tilde{\sigma}_{ik}\,n_k+\left(P^0-\frac{\sigma}{R}\right)n_i\right]S_{ij}\,\mathrm{d}S$$

$$-\frac{1}{4\pi\mu}\int_S \bar{u}_{\mathrm{N}}\,n_i G_{ij}\,\mathrm{d}S+\tfrac{1}{2}\bar{f}_i^n\,C_{ij}^n(\boldsymbol{x}_0)-\tfrac{1}{2}\bar{u}_{\mathrm{T}}^l\,D_j^l(\boldsymbol{x}_0). \tag{22}$$

For the calculations in the present article we tested several of the above procedures, comparing their efficiency and convergence. Strategies A and B, both implemented with Newton's iteration, where in the second case the iteration is based on the normal-stress method, proved successful for a variety of geometries and in a wide range of Bond numbers $B = \rho g/\sigma k^2$. In general, for a moderate number of segments ($N \sim L \sim 30$) the two methods required comparable computational effort. For larger numbers of points, the former method became significantly more expensive owing to the increased size of the final system. However, at low flow rates, strategy A had a larger radius of convergence.

Strategy A, coupled with Youngren & Acrivos' (1976) technique, was moderately successful, with limited and slow convergence, especially at low Bond numbers (high surface tension). In addition, it was very sensitive to the choice of ancillary linear systems and final iteration residuals. Similar difficulties were encountered by Youngren & Acrivos (1976) who had to resort to optimization techniques to accelerate convergence.

Strategy B with Ryskin & Leal's (1984*a*) iteration technique did not converge, although admittedly, we did not devote much effort to refine the iteration procedure.

Additional difficulties were encountered when the free surface was very deformed, and when its slope dy/dx was locally pronounced. The first is attributed to the inadequate spatial resolution associated with our limited computational resources. The second is attributed to the very nature of our numerical representation, requiring a unique correspondence between the x- and y-coordinates of the surface marker points. The latter difficulty may be readily alleviated by adopting a higher-order representation, for instance using spine parametrization (Kistler & Scriven 1983). It should be noted that for the above problematic cases, the calculations did converge, but the free-surface profile contained small-amplitude irregularities.

With respect to the basic flow, two choices were considered, namely

$$\tilde{u} = -\frac{g}{2\nu}\sin \alpha y, \quad \tilde{P} = -\rho g \cos \alpha y, \tag{23}$$

and

$$\tilde{u} = -\frac{g}{2\nu}\sin \alpha y(y-2w), \quad \tilde{P} = -\rho g \cos \alpha (y-w), \tag{24}$$

where w is the film height at the beginning of a flow cell (figure 3). Although the choice of basic flow does not affect the accuracy of the solution, it does affect the convergence of the numerical scheme. We found that for a moderate numbers of points, the first choice offers a larger radius of convergence, especially at low flow rates.

To clarify certain issues of the computational procedure, we note that the curvature at the free surface was evaluated using cubic-spline interpolation. The singular integrals defined above were evaluated by subtracting off the singularities, as explained in Pozrikidis (1987). Finally, to ensure that the calculations produced a physically acceptable solution, the calculated disturbance boundary force was integrated along the boundary of a flow period, and was seen to vanish with increasing the number of points. Our numerical results did not indicate multiplicity of solutions, although a formal analysis of the Jacobian matrix was not performed.

With respect to the initial guesses, continuation of the free-surface profile with respect to flow rate was employed. When a reasonably accurate initial guess for the free surface was available, the Jacobian matrix was calculated only once, at the first

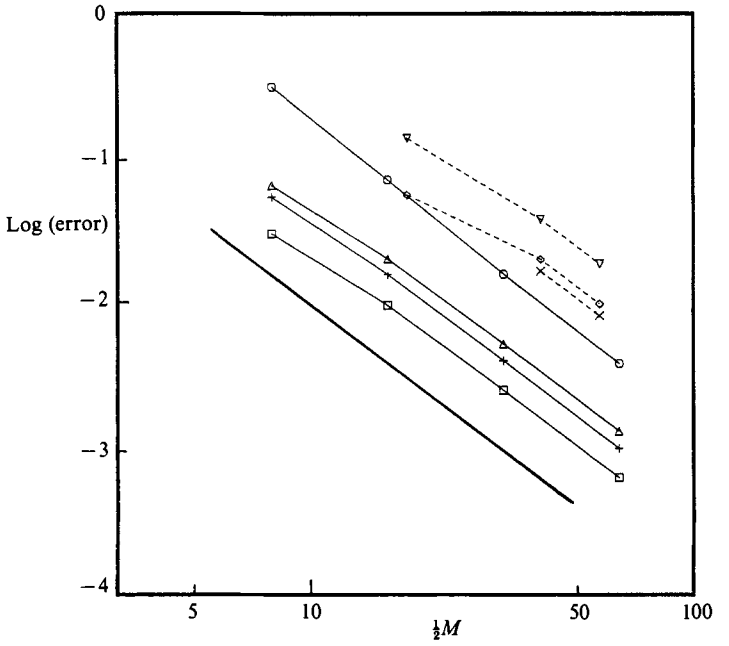

FIGURE 2. Relative error as a function of total number of segments $M = N + L$. Heavy solid line indicates a slope of -2. Continuous lines correspond to sinusoidal wall with $\alpha = 45°$, $a/\lambda = 0.200$, $w/\lambda = 0.100$ (see figure 4*c*). Dashed lines correspond to wall with square cavities shown in figure 16. The different curves correspond to the y-position of free surface: □, ×, $x = \frac{1}{2}\lambda$; ○, ◇, $x = 0$; △, $x = -\frac{1}{2}\lambda$, and to the disturbance x-force along one period of the wall: +, ▽.

iteration, and then it was kept constant throughout the calculations. All computations were performed on an IBM 3090 computer, with a typical CPU time for every calculation in the order of 10 minutes.

3.1. *Numerical error*

The error introduced by the above discretization is discussed in detail by Higdon (1985). Here, we mention in passing that for a flow with smooth boundaries, the error is $O(\delta^2)$, where δ is the boundary segment length. For flow with sharp corners, the error becomes $O(\delta)$ for segments in the neighbourhood of the corner, and $O(1)$ for segments adjoining the corner. Higdon showed that the corner error is of local nature and, therefore, it has little effect on the solution far away from the singular region. In practice, to minimize the error associated with a corner one may use a high local density of boundary segments, a policy followed in our calculations.

To demonstrate that the overall error is indeed $O(\delta^2)$, in figure 2 we present a series of data for flow over a sinusoidal wall (figure 4*c*), as well as for flow along a wall with square cavities (figure 16). In general, for flow on the sinusoidal wall, we found that 32 segments ($N = L = 32$) along the solid wall and the free surface are sufficient to define the free-surface profile within plotting accuracy. However, when the free surface developed regions of high curvature, a larger number of free-surface segments was introduced. The maximum number of segments used in the present calculations was $N = L = 64$.

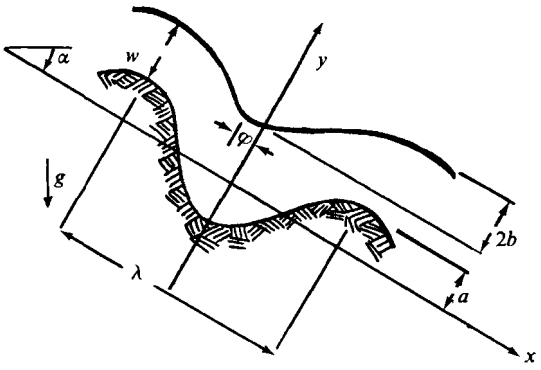

FIGURE 3. Flow of a liquid film along a wavy wall: schematic representation.

4. Flow along a sinusoidal wall

We study the flow of a liquid film along an inclined sinusoidal wall defined by

$$y = -a\cos(kx), \tag{25}$$

where the x-axis forms an angle α with respect to the horizontal (figure 3). This geometry is particularly convenient from an analytical standpoint, as it allows a comparison of numerical results with asymptotic analysis, and is free of singularities associated with wall corners.

In non-dimensional variables, the flow may be specified by the reduced wall amplitude a/λ, the inclination angle α, the equivalent film thickness for a perfectly smooth wall β/λ defined by (29) (a measure of flow rate), and the Bond number $B = \rho g/\sigma k^2$. For numerical convenience however, we introduce an additional variable expressing the film thickness at the crest of the wavy wall w/λ (figure 3). In this fashion, and assuming there is a unique correspondence between w/λ and β/λ, we specify the flow by the two geometrical parameters, α, a/λ, the flow-rate parameter w/λ, and the Bond number.

In the above definitions we assumed that gravity is normal to the generators of the wavy wall. In fact, this is not a necessary restriction. In the general case, the gravity vector may be decomposed into a component normal to and a component parallel to the generators. The flows associated with these two components are independent, with the shape of the free surface determined exclusively by the flow normal to the generators, as discussed in the previous section. The component along the generators simply causes a lateral drift of fluid particles, a subject outside the scope of the present work.

4.1. *Free-surface profiles*

First, we analyse flow without capillary forces, $B = \infty$, concentrating on the effect of wave amplitude, inclination angle and flow rate. As a starting point, we examine flow along a wall of moderate amplitude $a/\lambda = 0.100$, inclined at an angle of $\alpha = 45°$. Before considering the numerical results, it is instructive to consider the two limiting cases of very large and very small flow rates. For large flow rates, we expect that the waviness of the solid wall will cause only a slight deflection of the free surface from the planar shape. For small flow rates, we expect that the liquid film will closely follow the profile of the wavy wall. This behaviour is indeed verified by figure 4(*a*), where we present a family of free-surface profiles. For intermediate flow rates, the free surface is a nearly sinusoidal wave whose amplitude decreases with increasing

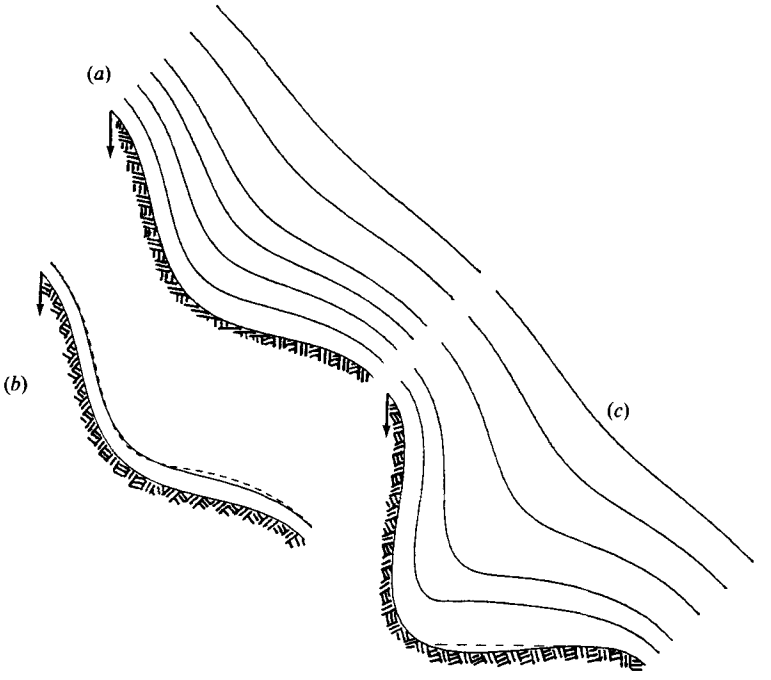

FIGURE 4. Free-surface profiles for flow over a wavy wall with (*a*) inclination $\alpha = 45°$, wave amplitude $a/\lambda = 0.100$, and in decreasing order $w/\lambda = 0.400, 0.300, 0.200, 0.150, 0.100, 0.050$ or $\beta/\lambda = 0.444, 0.338, 0.230, 0.173, 0.114, 0.055$; (*b*) as in (*a*) but with $w/\lambda = 0.0350$ or $\beta/\lambda = 0.0378$, where the dashed line shows predictions of asymptotic theory for small flow rates; (*c*) $\alpha = 45°$, $a/\lambda = 0.200$, and in decreasing order $w/\lambda = 0.400, 0.300, 0.200, 0.100, 0.050$ or $\beta/\lambda = 0.457, 0.351, 0.243, 0.122, 0.059$.

flow rate. There is a phase shift between the free surface and the wall that appears to be a non-monotonic function of flow rate. To clarify our graphical description, we stress that free surfaces will be represented with solid lines, and streamlines with dashed lines.

Figure 4(*a*) shows that for very low flow rates, the film thickness tends to zero throughout the wall, in a uniform manner. It appears then reasonable to speculate that the flow tends to a state of local equilibrium where the velocity is locally tangent to the wall with a parabolic profile,

$$u = \frac{g_T}{2\nu} z(2h - z), \tag{26}$$

where z is in a direction normal to the wall, h is the local film thickness, and g_T is the gravity component tangent to the wall, given by

$$g_T = \frac{g \sin\alpha[1 - (ka)\cot\alpha \sin kx]}{(1 + (ka)^2 \sin^2 kx)^{\frac{1}{2}}}. \tag{27}$$

The leading approximation to the free-surface profile may be inferred from a simple mass balance using (26). In terms of local film thickness this gives

$$\frac{h}{\beta} = \left(\frac{g}{g_T}\right)^{\frac{1}{3}}, \tag{28}$$

where

$$\beta = \left(\frac{3\nu Q}{g \sin\alpha}\right)^{\frac{1}{3}} \tag{29}$$

is the equivalent film thickness for a perfectly smooth wall, and Q is the flow rate.

The above heuristic description may be put into a formal context of an asymptotic expansion, valid for small values of the parameter $\epsilon = h/r$, where r is the minimum radius of curvature of the wall. The analysis, undertaken by Wang (1984), reveals that indeed (26)–(29) provide the leading approximation to the flow. It also shows the rather interesting result that except in cases of excessively high surface tension, inertial and capillary effects make an order-ϵ contribution to the free-surface profile.

To examine the consistency between the numerical and the above asymptotic results, in figure 4(*b*) we plot a free-surface profile for a quite low flow rate, and compare it with the one predicted by (28). We observe a very good agreement that is expected to improve at lower flow rates. Note that the asymptotic theory overestimates the film thickness in the decelerating zone. Unfortunately, calculations for lower flow rates were prohibited by increased computational cost.

Now we would like to examine the free-surface profile for other wave amplitudes, maintaining the inclination angle at a constant value, $\alpha = 45°$. For very small a/λ our results are in very good agreement with the asymptotic analysis of Wang (1981) that is valid for small wave amplitudes and large flow rates, i.e. small a/λ and large w/λ. This analysis predicts that the free surface is a perfect sinusoidal wave whose amplitude and phase are functions of flow rate. To illustrate the behaviour for large wave amplitudes, we present a series of free-surface profiles for $a/\lambda = 0.200$, figure 4(*c*). As previously, for large and moderate flow rates, the free surface is a nearly symmetric, sinusoidal wave. For low flow rates however, nearly stagnant regions of fluid develop, and the free surface becomes horizontal over the right-hand portion of each flow cell. In the limit of zero flow rate, the flow domain is not depleted of fluid. The limiting configuration consists of a pool of static fluid that wets part of the solid wall, as indicated by the dashed line in figure 4(*c*).

We wish now to consider the free-surface profile in a more quantitative fashion. This will help us gain some physical insight and will provide a basis for comparison with asymptotic analysis. For this purpose, we define the amplitude b and phase φ of the free surface, as shown in figure 3. In figure 5(*a*, *b*) we plot these quantities as functions of β/λ. Figure 5(*a*) clearly illustrates the rapid decrease in the free-surface amplitude with increasing β/λ, i.e. increasing the flow rate. Figure 5(*b*) shows that φ is always negative, implying increased film thickness along the right-hand side of each flow period. As the flow rate is increased, the phase increases rapidly, reaches a maximum, and then decreases in a monotonic fashion. For large flow rates, φ tends to zero, indicating that the free surface tends to become in phase with the wavy wall. In figure 5(*a*, *b*) (dashed lines), we also show predictions of the asymptotic analysis of Wang (1981). For small wave amplitudes, the agreement between the numerical and the asymptotic results is excellent, even at very low flow rates (where the asymptotic analysis is expected to break down). For large wave amplitudes, the asymptotic analysis overestimates the effect of the wall waviness on the deflection of the free surface, particularly at high flow rates.

We saw that at high flow rates, the free surface is always a sinusoidal wave, whereas at low flow rates, it follows the shape of the solid wall and may yield pools of nearly static fluid. Although these results were derived with reference to a 45° inclination angle, our calculations show that they remain qualitatively valid for other wall orientations. As an example, in figure 6(*a*, *b*) we present free-surface profiles for $\alpha = 9°$, and for wave amplitudes $a/\lambda = 0.100$ and 0.200. In addition, in

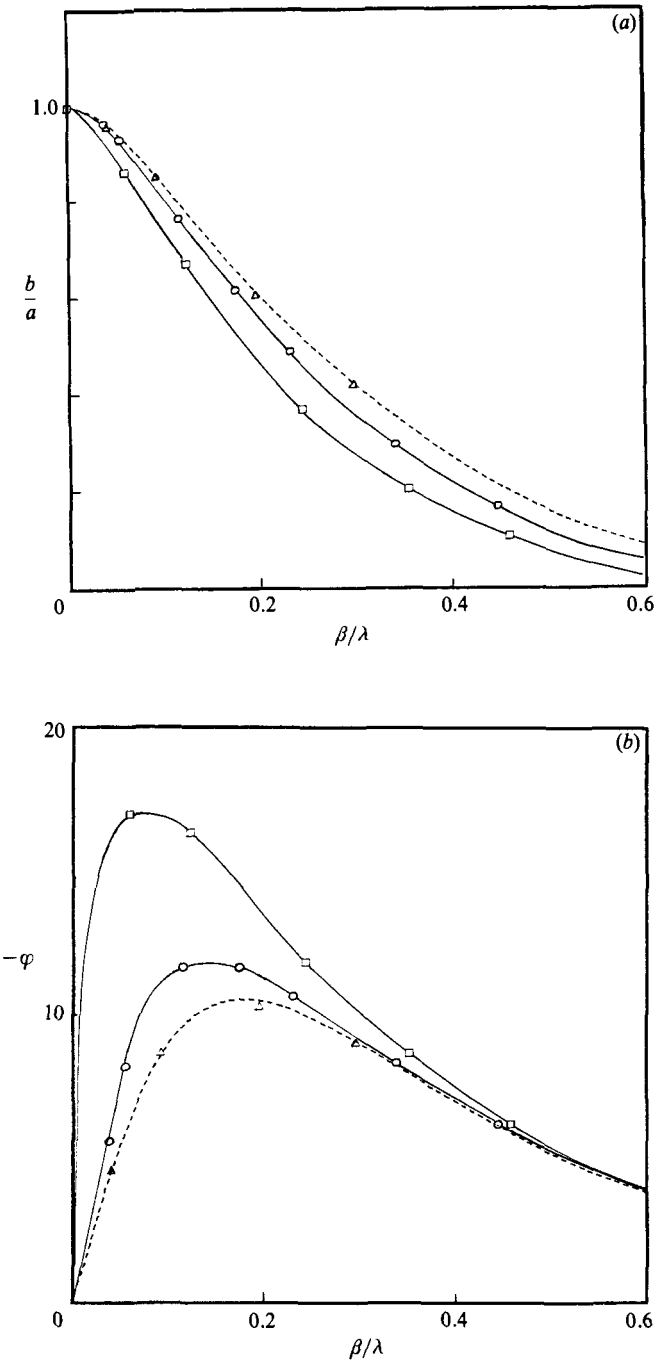

FIGURE 5. (*a*) Amplitude and (*b*) phase shift of the free surface as a function of the flow rate parameter β (equation (29)), for inclination angle $\alpha = 45°$ and different wave amplitudes: △, $a/\lambda = 0.010$; ○, 0.100; □, 0.200; dashed line shows predictions of asymptotoic theory for small a/λ and a/w (Wang 1981).

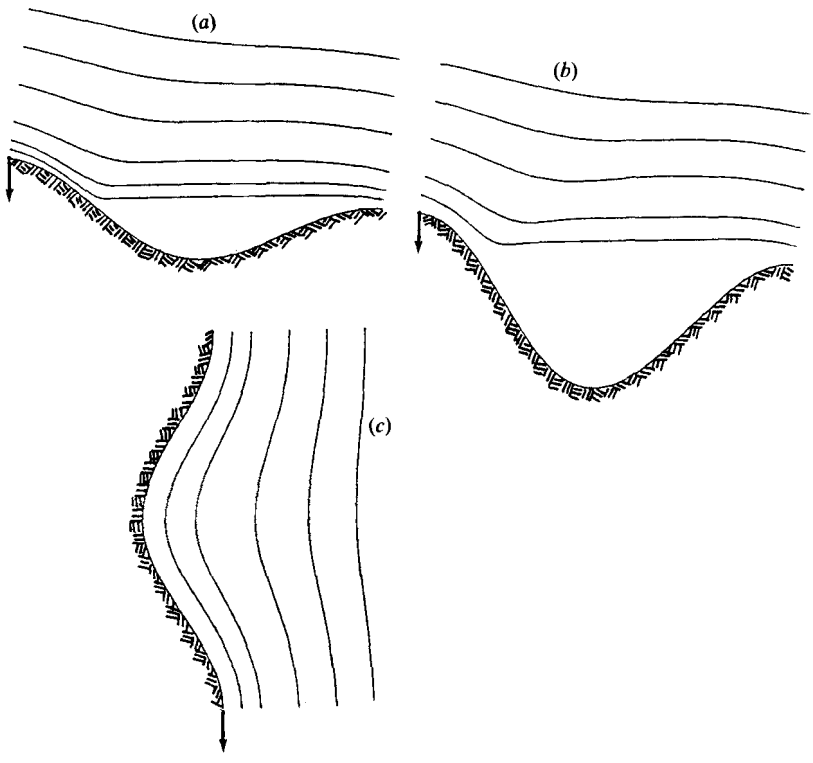

FIGURE 6. Free-surface profiles for flow over a wavy wall of (*a*) $\alpha = 9°$, $a/\lambda = 0.100$, and $w/\lambda = 0.400, 0.300, 0.200, 0.100, 0.050, 0.025$ or $\beta/\lambda = 0.448, 0.346, 0.242, 0.129, 0.064, 0.032$; (*b*) $\alpha = 9°$, $a/\lambda = 0.200$, and $w/\lambda = 0.400, 0.300, 0.200, 0.100, 0.050$ or $\beta/\lambda = 0.461, 0.360, 0.256, 0.140, 0.069$; (*c*) $\alpha = 90°$, $a/\lambda = 0.100$, and $w/\lambda = 0.400, 0.300, 0.200, 0.100, 0.050$ or $\beta/\lambda = 0.444, 0.338, 0.229, 0.113, 0.054$.

figure 6(*c*) we show profiles for a vertical wall with amplitude $a/\lambda = 0.100$. Note that in this case, the free surface is symmetric with respect to the origin and, thus, the phase shift is equal to zero.

4.2. *Structure of the flow*

In the previous section we discussed the shape of the free surface as a function of wall orientation, wave amplitude, and flow rate. This gave us some insight into the physics of the motion by revealing regions of thin-film flow and regions of nearly stagnant fluid. In this section we would like to consider in more detail the structure of the flow, concentrating on the wall shear stress and streamline pattern.

The distribution of shear stress along the wall is important in processes involving heat or mass transfer and deposition or dissolution of materials at high Prandtl or Schmidt numbers. For instance, in the case of material deposition, the wall shear stress dictates the location and orientation of emerging patterns. Similarly, in the case of wall dissolution, the wall shear stress determines the shape of forming cavities. Further, high shear stress implies effective removal of particles or bubbles that might exist as impurities in industrial fluids. Thus, from an equipment design standpoint, one would like to optimize the wall geometry to maintain the wall shear stress above a specified minimum level. Finally, the wall shear stress indicates onset of recirculating fluid regions; a change in sign of the wall shear stress marks flow reversal. Onset of viscous eddies is interesting from a fundamental standpoint (see for

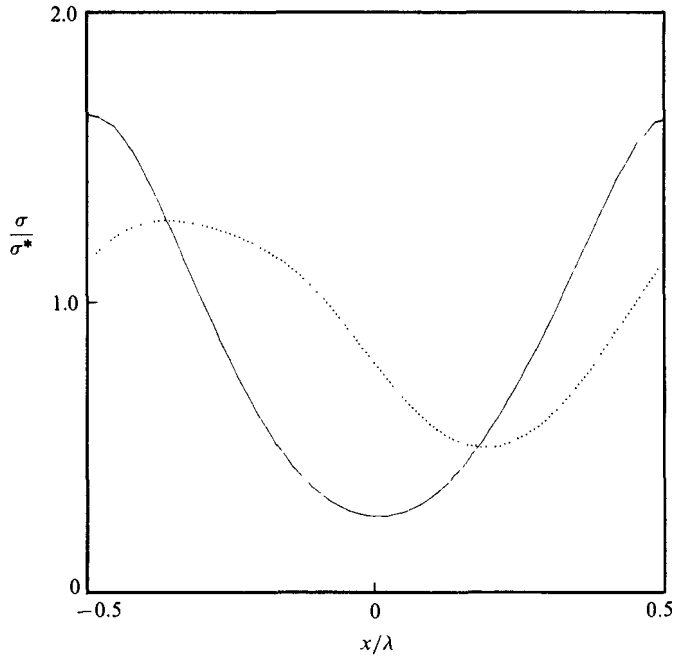

FIGURE 7. Shear stress along a wavy wall of $a/\lambda = 0.100$ and $\alpha = 45°$, reduced by the corresponding value σ^* at the same flow rate but for a perfectly plane wall; ——, $w/\lambda = 0.500$; · · · · · ·, 0.050.

instance Hasimoto & Sano 1980), but also from a practical standpoint, as it may locally inhibit the rate of heat or mass transport.

Let us first consider the wall-shear-stress distribution along a wall of amplitude $a/\lambda = 0.100$, inclined at an angle of 45°. Free-surface profiles for this geometry were presented in figure 4(*a*). In figure 7 we plot the wall shear stress for two characteristic cases. Note that the shear stress is reduced with respect to the wall shear stress for the same flow rate but, for a perfectly plane wall, $\sigma^* = \rho g \beta \sin \alpha$. For high flow rates, the shear stress has a sinusoidal form in phase with the wavy wall. It reaches a maximum at the crest and a minimum at the trough. This is due to the acceleration and deceleration of the fluid above the wave crest and trough respectively, merely for mass conservation. This behaviour is similar to that of flow in confined wavy channels (Pozrikidis 1987), consistent with the fact that at high flow rates, the presence of the free surface does not affect the flow in the vicinity of the wall. At lower flow rates, the shear stress maintains its sinusoidal form, but its maximum is shifted toward the trough. At very low flow rates, the shear stress scales with the local film thickness. For the flow corresponding to the dotted curve in figure 7, the maximum and minimum shear stress occur at approximately $x/\lambda = -0.25$ and $x/\lambda = 0.25$, where the gravity component tangent to the wall (and hence the film thickness) reach extreme values. In this case, the shear stress may be approximated as a sinusoidal wave which is shifted by 45° with respect to the wall. For both cases shown in figure 7, the wall shear stress is positive implying that flow does not reverse direction. Furthermore, our calculations show that the tangential velocity at the free surface scales with the wall shear stress and by extension, with the local film thickness. Thus, it may be readily inferred from the free-surface profiles, using a simple mass balance.

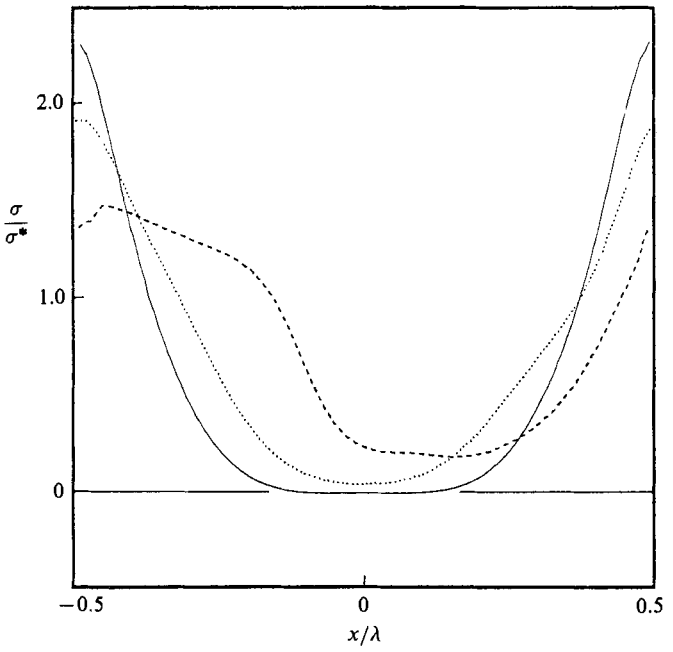

FIGURE 8. Shear stress along a wavy wall of $a/\lambda = 0.200$ and $\alpha = 45°$; ——, $w/\lambda = 0.400$; · · · · ·, 0.200, – – – –, 0.050.

Next, we examine the wall sheer stress for larger wave amplitudes, focusing on the case $\alpha = 45°$, $a/\lambda = 0.200$ (figure 8). Free-surface profiles for this geometry were described in figure 4(*c*). As in the small-amplitude case, at large flow rates (solid curve), the shear stress is a nearly symmetric wave, in phase with the wall. It becomes negative over a small region centred at the trough, indicating flow reversal. At lower flow rates, the sheer stress becomes notably asymmetric (dotted curve). It remains positive throughout the wall, indicating that flow reversal may be suppressed by sufficiently decreasing the flow rate. Finally, at very low flow rates (dashed curve) the wall shear stress obtains a rather irregular shape. It reaches a maximum at some point near the wave crest and becomes flat around the trough. Maximum shear stress occurs at the region of thin-film flow, near the crest of the wavy wall. Minimum shear stress occurs at the nearly stagnant-fluid region, in the vicinity of the trough. As previously, the free-surface velocity scales with the wall shear stress. Streamline pattens for the three cases discussed above are shown in figure 9(*a–c*). We observe that flow reversal occurs only when the flow rate exceeds a critical value. It should be emphasized that flow reversal is due to the increased thickness of the film rather than to inertial effects, which are completely absent.

At this point, we would like to emphasize the implications of the above results in certain engineering processes. As an example, we consider chemical etching of a dissolving wall. In this case, the location and shape of forming cavities is affected by the distribution of wall shear stress, and our results show that they may be effectively monitored by controlling the flow rate.

The behaviour for other inclination angles is similar to that discussed above. The shear stress is increased at regions of thin-film flow and reduced at regions of accumulated fluid. Flow reversal occurs above a critical wave amplitude, and then only for sufficiently high flow rates. The critical flow rate for flow reversal decreases

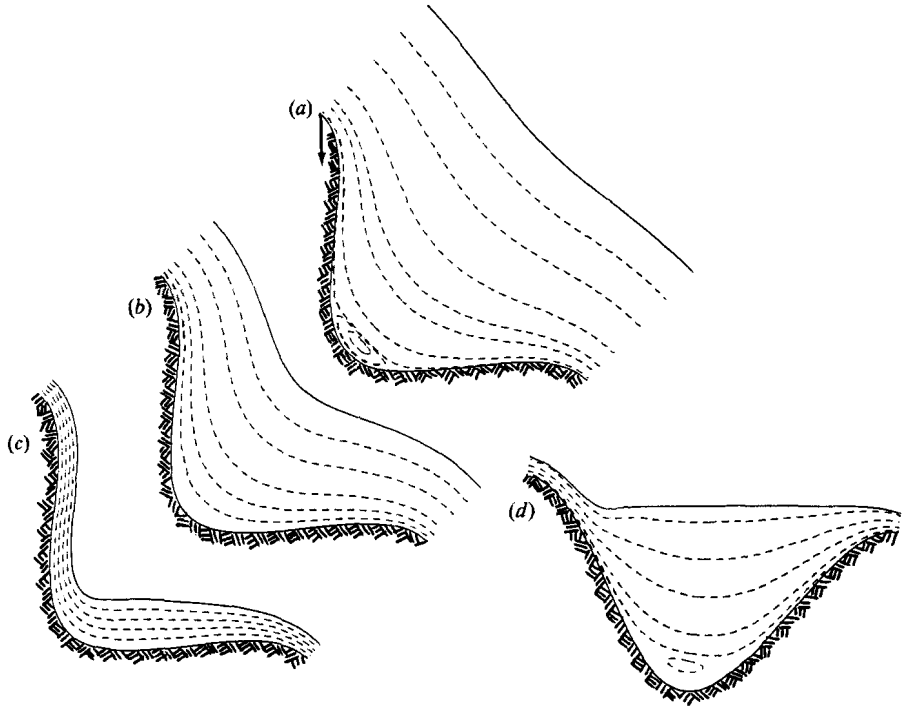

FIGURE 9. Streamline patterns for flow over a wall of (*a–c*) $\alpha = 45°$, $a/\lambda = 0.200$, and (*a*) $w/\lambda = 0.400$, (*b*) $w/\lambda = 0.200$, (*c*) $w/\lambda = 0.050$, (*d*) $\alpha = 9°$, $a/\lambda = 0.250$, $w/\lambda = 0.050$.

as the wave amplitude is increased, and vanishes for very large wave amplitudes. To validate the above conclusions, in figure 10 we present the wall shear stress and surface tangential velocity for $\alpha = 9°$, and $a/\lambda = 0.200$ (the corresponding free-surface profile was shown in figure 6*b*). Notice that both the shear stress and the surface velocity peak approximately at the neck, where the thin film discharges into the almost stagnant pool. The shear stress becomes negative over a very small region inside the wave trough, indicating a small region of reversed flow. Finally, to show that eddies may develop even at low flow rates, provided the wave amplitude is sufficiently large, in figure 9(*d*) we show the streamline pattern for $\alpha = 9°$, $w/\lambda = 0.250$. For even larger wave amplitudes we expect onset of a series of alternating self-similar eddies as described by Moffatt 1964 (see also Pozrikidis 1987).

4.3. *Effect of surface tension*

In this section we discuss the effect of surface tension on the free-surface profile and the structure of the flow. Physically, we expect that for constant flow rate, increasing the surface tension will cause a decrease of the deflection of the free surface from the planar shape. This is indeed verified by the asymptotic analysis of Wang (1981) as well as by our numerical results for small-amplitude corrugations, figure 11(*a*). Figure 11(*b*) shows a rapid increase of the phase φ with decreasing the Bond number, a result not intuitively obvious.

The results in figure 11(*a*) appear to indicate that as the flow-rate parameter β/λ is decreased, the amplitude of the free surface tends to that of the wavy wall and the film thickness vanishes in a uniform fashion. To see whether this is true for all cases, in figure 12(*a–c*) we present a sequence of free-surface profiles for finite wall

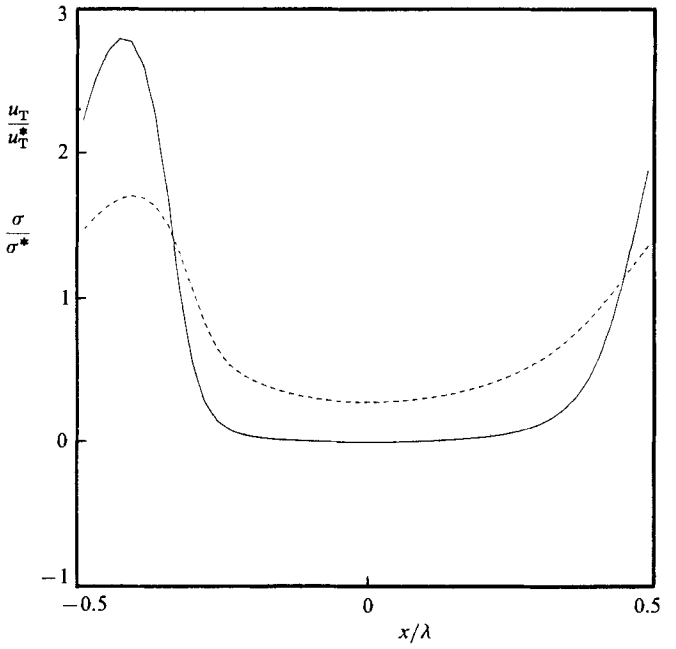

FIGURE 10. Shear stress along the wavy wall (——) and free-surface velocity (– – –) for $\alpha = 9°$, $a/\lambda = 0.200$, $w/\lambda = 0.050$. The velocity is reduced by the corresponding value u^* at the same flow rate but for a perfectly plane wall.

corrugations, $a/\lambda = 0.200$, $\alpha = 45°$, decreasing the Bond number. We observe that at finite Bond numbers (figure 12*b*, *c*), as the flow rate is decreased, the amplitude of the free surface does not tend to that of the solid wall but to a smaller value. To demonstrate this clearly, in figure 13(*a*, *b*) we plot the free-surface amplitude and phase shift, respectively, as functions of flow rate. It is interesting to observe the failure of asymptotic analysis of Wang (1981), even in a qualitative sense, for moderate or low flow rates, at finite Bond number. However, this is to be expected since the asymptotic theory ceases to be valid when the mean film thickness becomes comparable with the amplitude of the wall.

The above observations motivate a closer consideration of the asymptotic flow structure for small flow rates. We saw that in this limit the flow is composed of a thin liquid film which may connect periodic pools of nearly stagnant fluid. As the flow rate is decreased, the thickness of this film tends to zero and, thus, the asymptotic configuration is either depleted of fluid or composed of periodic pools of static liquid. The shape of the free surface bounding each pool is basically determined by a balance between capillary and gravity forces.

$$kh \sim \frac{1}{B}\frac{1}{kR} + c, \tag{30}$$

where h is measured in the direction of the body force with origin at $x = y = 0$, c is a constant, and

$$\frac{1}{R} = \frac{y''}{(1+y'^2)^{\frac{3}{2}}}, \tag{31}$$

where y describes the free surface, and the derivatives are with respect to x. To show this clearly, in figure 14 we plot the non-dimensional capillary force $1/kRB$ versus

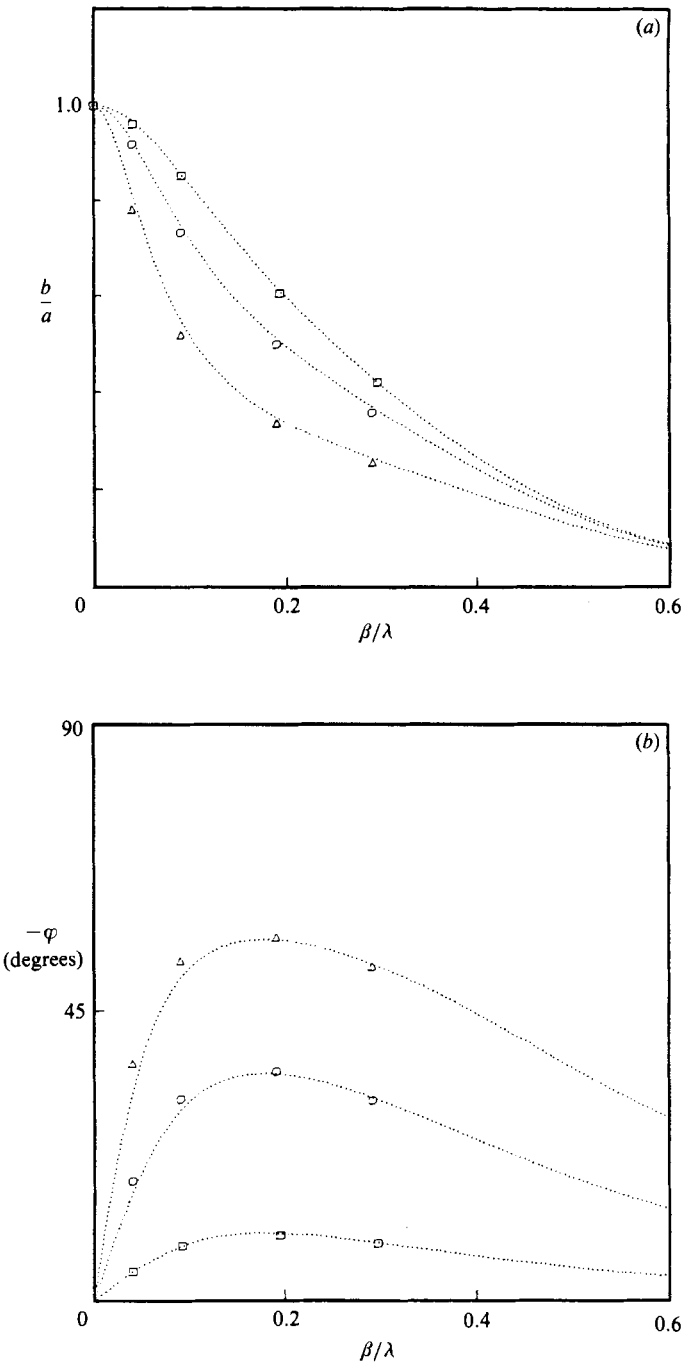

FIGURE 11. Effect of flow rate on the (*a*) amplitude and (*b*) phase shift of free surface, parametrized by the Bond number, for $\alpha = 45°$, $a/\lambda = 0.010$, and □, $B = \infty$; ○, 0.5; △, 0.2. Dotted lines show predictions of asymptotic theory for small a/λ and large β/λ (Wang 1981).

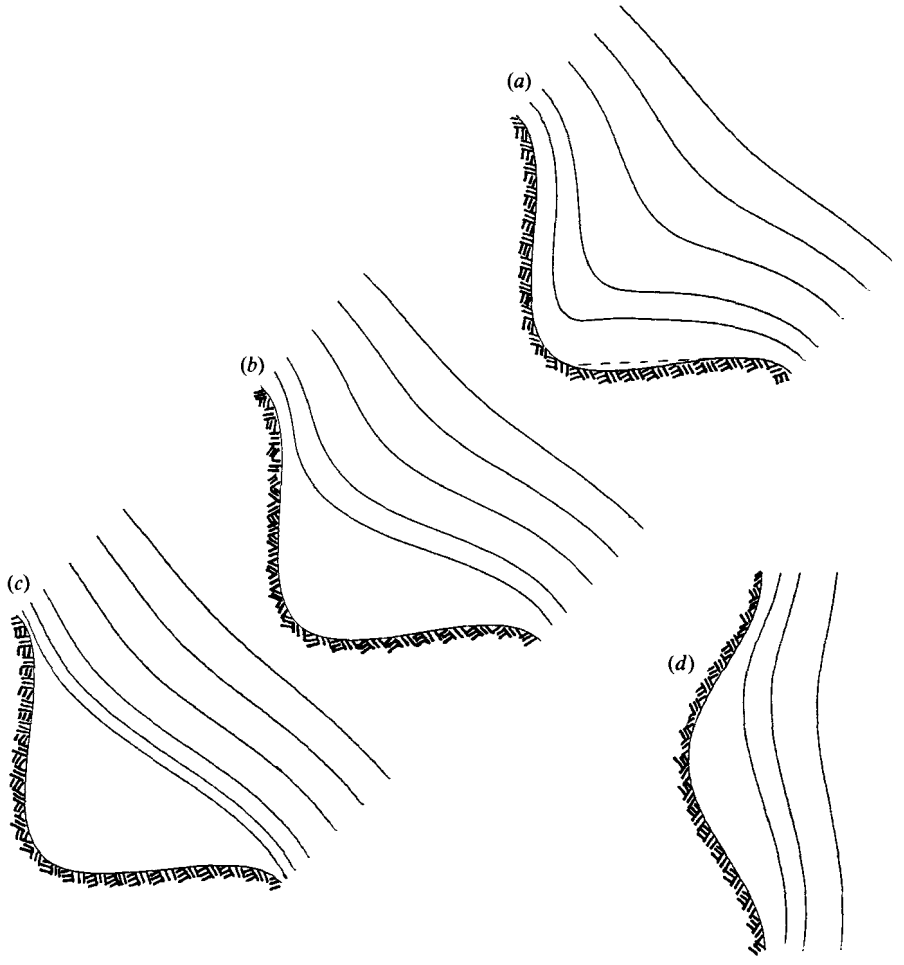

FIGURE 12. Free-surface profiles for a wavy wall of $\alpha = 45°$, $a/\lambda = 0.200$ for different flow rates. The sequence (*a–c*) shows the effect of surface tension: (*a*) $B = \infty$ and $w/\lambda = 0.400, 0.300, 0.200, 0.100, 0.050$ or $\beta/\lambda = 0.457, 0.351, 0.243, 0.122, 0.0591$; (*b*) $B = 0.5$ and $w/\lambda = 0.400, 0.300, 0.200, 0.100, 0.050$ or $\beta/\lambda = 0.459, 0.355, 0.248, 0.125, 0.053$; (*c*) $B = 0.2$ and $w/\lambda = 0.400, 0.300, 0.200, 0.100, 0.050, 0.020$ or $\beta/\lambda = 0.463, 0.361, 0.258, 0.145, 0.079, 0.032$; (*d*) $B = 0.2$ and $\alpha = 90°$, $a/\lambda = 0.100$, and $w/\lambda = 0.200, 0.100, 0.050$ or $\beta/\lambda = 0.239, 0.125, 0.057$ (compare with figure 6*c*).

the gravity force kh along the free surface for two of the flows depicted in figure 12. In the region of nearly stagnant fluid we observe a linear relationship with slope equal to unity, indicating the insignificance of viscous forces. Within the thin film, viscous stresses make an important contribution. At infinite Bond number, capillary forces are absent and, therefore, (30) shows that the free surface bounding a stagnant pool must be a straight horizontal line which intersects the solid wall on one end and is horizontal to it on the other (h is constant). From the point of view of hydrostatics, this configuration accommodates the maximum amount of static fluid. At finite Bond numbers, however, both sides of (30) become important and the asymptotic free-surface profile is determined by the second-order differential equation (30) subject to two boundary conditions. Since from a hydrostatics viewpoint these conditions may be arbitrary, there is an infinity of possible asymptotic configurations. For instance, forcing the free surface to pass through two

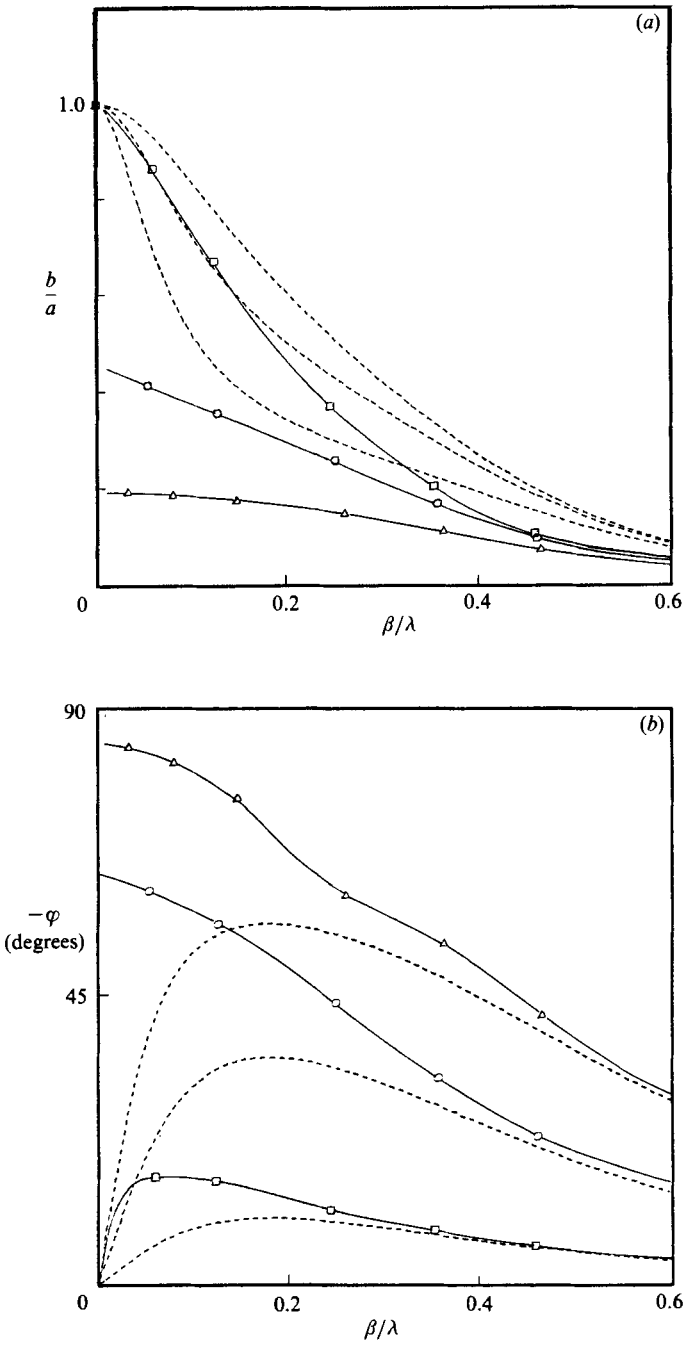

FIGURE 13. Effect of Bond number on the (*a*) amplitude and (*b*) phase shift of the free surface as functions of flow rate for a wavy wall of inclination angle $\alpha = 45°$, wave amplitude $a/\lambda = 0.200$, and: □, $B = \infty$; ○, 0.5; ▽, 0.2. Dashed lines show predictions of asymptotic theory for small a/λ and large β/λ (Wang 1981).

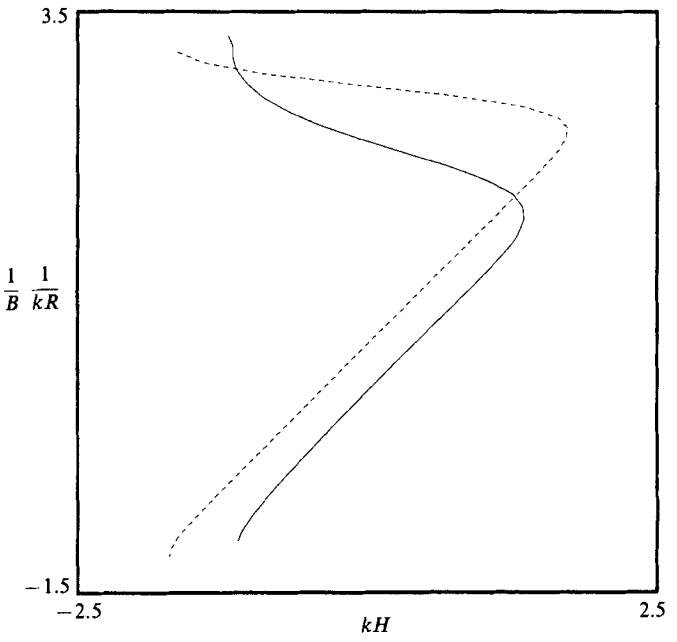

FIGURE 14. Capillary versus gravity forces along the free surface for $a/\lambda = 0.200$ and $\alpha = 45°$, for: ——, $B = 0.5$, $w/\lambda = 0.050$ and – – –, $B = 0.2$, $w/\lambda = 0.020$.

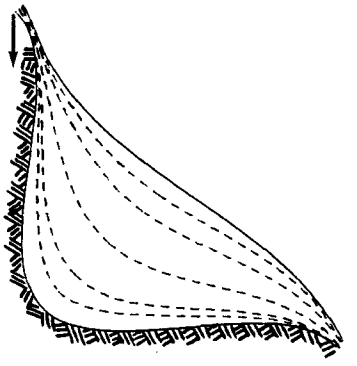

FIGURE 15. Streamline pattern of flow over a wavy wall of inclination $\alpha = 45°$, amplitude $a/\lambda = 0.200$, and film thickness $w/\lambda = 0.020$, for $B = 0.2$.

arbitrarily selected points along the wall yields a family of profiles which are acceptable provided they do not cross the wall. The true asymptotic configuration however may be found only be means of an exact asymptotic analysis for the specific wall geometry, similar to that of Ruschak & Scriven (1977). Here, we must note that the analysis of Wang (1984), valid for low flow rates, may not be applied, since the film thickness is not uniformly small along the wall.

It is important to not that for very thin films, molecular forces come into play and these may substantially alter the physics of the motion. For example, these forces require a contact angle at the solid–gas–liquid contact line, characteristic of the fluid/solid physico–chemical interaction. If the asymptotic hydrodynamic contact angle is not equal to this static contact angle, oscillatory or unsteady motion may set up. Analysis of this motion would provide an interesting topic for research.

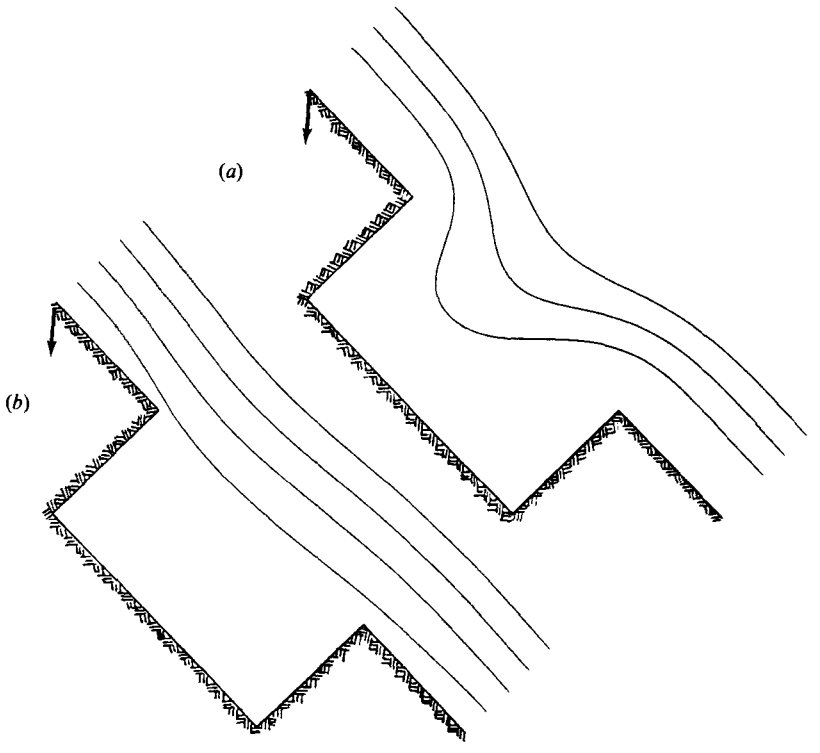

FIGURE 16. Free-surface profiles for flow over a wall with a sequence of square cavities of aspect ratio 2. (*a*) $B = \infty$, and $w/\lambda = 0.2000, 0.1500, 0.1000$ or $\beta/\lambda = 0.2053, 0.1548, 0.1027$; (*b*) $B = 0.2$, and $w/\lambda = 0.2000, 0.1500, 0.1000, 0.050$ or $\beta/\lambda = 0.2130, 0.1606, 0.1051, 0.041$.

To illustrate the structure of the flow at finite Bond numbers, we present a characteristic streamline pattern (figure 15). Comparing this pattern to the ones shown in figures 9(*a–c*) for zero surface tension, demonstrates a stong effect of surface tension on the structure of the flow. Overall, increasing the surface tension moves the free surface away from the wave trough and, therefore, decreases the wall shear stress. In turn, this may lead to flow reversal, in agreement with the predictions of Wang (1984).

We conclude this section by noting that behaviour similar to the above is observed for other wall orientations. As an example, in figure 12(*d*) we present profiles for $\alpha = 90°$, $a/\lambda = 0.100$ and for $B = 0.5$. Observe that at the vertical orientation and for finite Bond numbers, the free surface is no longer symmetric with respect to the centre of each period (compare with figure 6*c*).

5. Flow along a wall with rectangular indentations

We studied the flow of a liquid film along a wavy wall partly as a means of extracting physical information about more general geometries. At this point we would like to demonstrate the accuracy of our conclusions as well as the generality of our numerical procedure. For this purpose, we discuss briefly flow over a wall with periodic rectangular indentations.

Figure 16(*a*) shows a sequence of three free-surface profiles for a cavities of aspect ratio 2 and for Bond number $B = \infty$. It is interesting to observe the pronounced

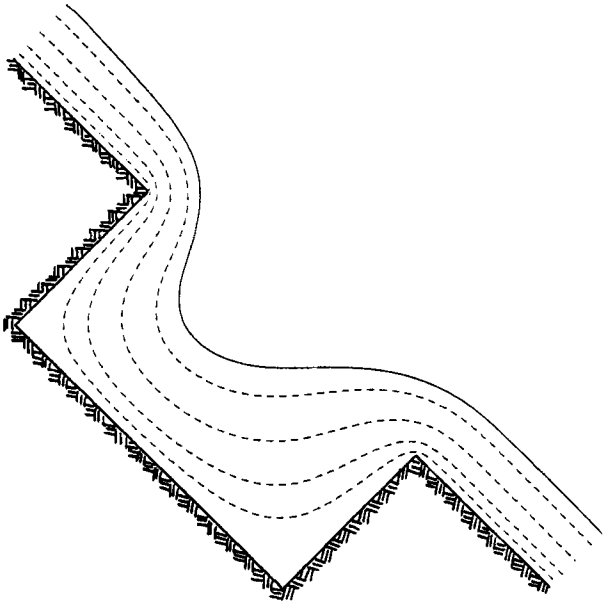

FIGURE 17. Streamline pattern for the lowest-flow-rate case shown in figure 16(*a*).

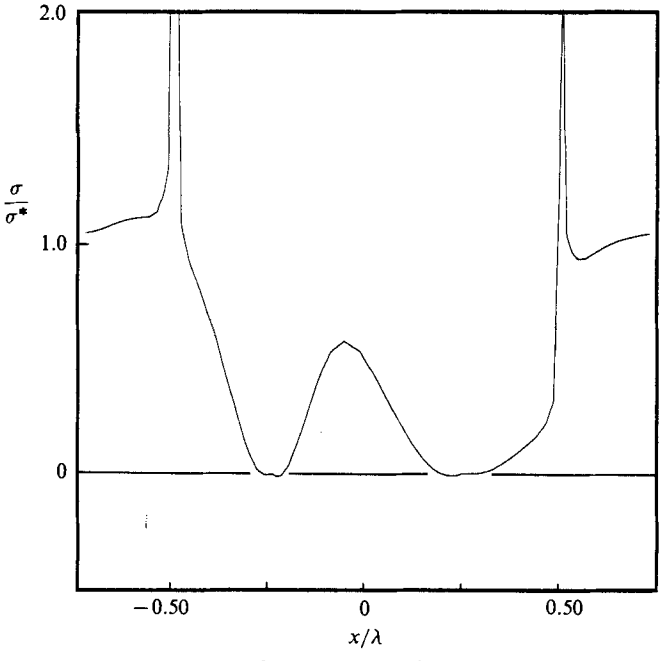

FIGURE 18. Wall shear stress for the lowest-flow-rate case shown in figure 16(*a*).

deformation of the free surface at low flow rates. Calculations for lower flow rates required an increased number of points leading to prohibitive computational cost. Figure 16(*b*) shows a sequence of free-surface profiles for the same geometry, but with increased surface tension, $B = 0.2$. Here, we observe a very small deformation of the free surface, even at very low flow rates.

Figure 17 illustrates the streamline pattern for the lowest-flow-rate case of figure

16(*a*). There are two series of small, self-similar eddies (Moffatt, 1964) at the two corners of the cavity which, however, are not detected with sufficient accuracy in the streamline pattern. Their presence is manifested in the wall-shear-stress distribution shown in figure 18; this obtains negative values over two very small regions centred on each cavity corner. It is interesting to observe the strong oscillations in the wall shear stress inside the cavity, indicative of regions of accelerating and regions of nearly stagnant fluid.

6. Concluding remarks

We have described a numerical method, based on the boundary-integral formulation, for analysing two-dimensional flows with free surfaces. The method is effective for flows with smooth boundaries as well as for flows with corners. Overall, our calculations verify the flexibility and efficiency of the boundary-integral formulation, and show that it constitutes an attractive alternative in the study of two-dimensional, viscous, free-surface problems.

Our calculations demonstrate a number of features for the flow of a liquid film along an inclined, periodic wall. Some of them may appear physically obvious, but others come as new insights. It is now appropriate to summarize certain results that make the most important contribution. First, we demonstrated that the wall-shear-stress distribution changes drastically with the flow rate, with subtle implications on the rate of simultaneous heat and mass transfer. Depending on the wall geometry, recirculating-flow regions may set up; these become more pronounced with increasing either the flow rate or the surface-tension coefficient. Finally, for finite surface tension, the asymptotic free-surface shape for very low flow rates depends on the overall wall geometry, and may be resolved only via an asymptotic expansion for the exact geometry.

Our calculations apply directly to the gravity-driven flow of a liquid film along an inclined wall. However, there are other situations where our results offer significant insights, including the flow of a thin liquid film on a rotating disk. This flow finds important applications in spin coating operations, and is exploited for the fabrication of optical disks and microelectronic components. In a spin coating process, a liquid film is distributed over a horizontal disk often containing concentric grooves, and is subsequently thinned by spinning the disk at high angular velocities (Higgins 1986). For small film thicknesses, and far away from the disk centre, the flow on an azimuthal plane is primarily driven by the centrifugal and the gravity force field. A simple analysis indicates that the centrifugal force is proportional to the radial distance from the disk centre. Now, to a first approximation, the centrifugal force may be approximated as constant over the length of a groove, and the local flow may be viewed as being driven by a uniform force field. The orientation of this field is a function of the radial distance from the disk centre. Under these assumptions, our calculations provide a local description of the spin coating process.

REFERENCES

CHIN, R. W., ABERNATHY, F. H. & BERTCHY, J. R. 1986 Gravity and shear wave instability of free surface flows. Part 1. Numerical calculations. *J. Fluid Mech.* **168**, 501–503.

DASSORI, C. G., DEIBER, J. A. & CASSANO, A. E. 1984 Slow two-phase flow through a sinusoidal channel. *Intl J. Multiphase Flow* **10**, 181–193.

FULFORD, G. D. 1964 The flow of liquids in thin films. *Adv. Chem. Engng* **5**, 151–236.

GELLER, A. S., LEE, S. H. & LEAL, L. G. 1986 The creeping motion of a spherical particle normal to a deformable interface. *J. Fluid Mech.* **169**, 27–69.

HASIMOTO, H. & SANO, O. 1980 Stokeslets and eddies in creeping flow. *Ann. Rev. Fluid Mech.* **12**, 335–363.

HIGDON, J. J. L. 1985 Stokes flow in arbitrary two-dimensional domains: shear flow over ridges and cavities. *J. Fluid Mech.* **159**, 195–226.

HIGGINS, B. G. 1986 Film flow on a rotating disk. *Phys. Fluids* **29**, 3522–3529.

HIRT, C. W., COOK, J. L. & BUTLER, T. D. 1970 A Lagrangian method for calculating the dynamics of an incompressible fluid with free surface. *J. Comp. Phys.* **5**, 103–124.

HIRT, C. W. & NICHOLS, B. D. 1981 Volume of fluid (VOF) method for the dynamics of free boundaries. *J. Comp. Phys.* **39**, 201–225.

KELMANSON, M. A. 1983 Boundary integral equation solution of viscous flows with free surfaces. *J. Engng Maths* **17**, 329–343.

KISTLER, S. F. & SCRIVEN, L. E. 1983 Coating Flows. In *Computational Analysis of Polymer Processing* (ed. J. R. A. Pearson & S. M. Richardson), chap. 8, pp. 243–299. Applied Science Publishers.

KRANTZ, W. B. & GOREN, S. L. 1970 Finite-amplitude, long waves on liquid films flowing down a plane. *Ind. Engng Chem.* **9**, 107–113.

LEE, S. H. & LEAL, L. G. 1986 Low Reynolds number flow past cylindrical bodies of arbitrary cross-sectional shape. *J. Fluid Mech.* **164**, 401–427.

MOFFATT, H. K. 1964 Viscous and resistive eddies near a sharp corner. *J. Fluid Mech.* **18**, 1–18.

PIERREHUMBERT, R. T. 1980 A family of steady, translating vortex pairs with distributed vorticity. *J. Fluid Mech.* **99**, 120–144.

POZRIKIDIS, C. 1987 Creeping flow in two-dimensional channels. *J. Fluid Mech.* **180**, 495–514.

RALLISON, J. M. 1984 The deformation of small viscous drops in viscous flows. *Ann. Rev. Fluid. Mech.* **16**, 45–66.

RALLISON, J. M. & ACRIVOS, A. A. 1978 A numerical study of the deformation and burst of a viscous drop in an extensional flow. *J. Fluid Mech.* **89**, 191–200.

RUSCHAK, K. J. & SCRIVEN, L. E. 1977 Developing flow on a vertical wall. *J. Fluid Mech.* **81**, 305–316.

RYSKIN, G. & LEAL, L. G. 1984*a* Numerical solution of free-boundary problems in fluid mechanics. Part 1. The finite-difference technique. *J. Fluid Mech.* **148**, 1–17.

RYSKIN, G. & LEAL, L. G. 1984*b* Numerical solution of free-boundary problems in fluid mechanics. Part 2. Buoyancy-driven motion of a gas bubble through a quiescent liquid. *J. Fluid Mech.* **148**, 18–36.

RYSKIN, G. & LEAL, L. G. 1984*c* Numerical solution of free-boundary problems in fluid mechanics. Part 3. Bubble deformation in an axisymmetric straining flow. *J. Fluid Mech.* **148**, 37–43.

TOUGOU, H. 1978 Long waves on a film flow of a viscous fluid down an inclined uneven wall. *J. Phys. Soc. Japan*, **44**, 1014–1019.

YOUNGREN, G. K. & ACRIVOS, A. 1976 On the shape of a gas bubble in a viscous extensional flow. *J. Fluid Mech.* **76**, 433–442.

WANG, C. Y. 1981 Liquid film flowing slowly down a wavy incline. *AIChE J.* **27**, 207–212.

WANG, C. Y. 1984 Thin film flowing down a curved surface. *Z. Angew. Math. Phys.* **35**, 533–544.